

## ARTICLE OPEN

Temperature-driven topological transition in 1T'-MoTe<sub>2</sub>

Ayelet Notis Berger<sup>1,2</sup>, Erick Andrade<sup>1</sup>, Alexander Kerelsky<sup>1</sup>, Drew Edelberg<sup>1</sup>, Jian Li<sup>3</sup>, Zhijun Wang<sup>4</sup>, Lunyong Zhang<sup>5,6</sup>, Jaewook Kim<sup>6</sup>, Nader Zaki<sup>7</sup>, Jose Avila<sup>8</sup>, Chaoyu Chen<sup>8</sup>, Maria C. Asensio<sup>8</sup>, Sang-Wook Cheong<sup>6</sup>, Bogdan A. Bernevig<sup>4,9,10,11</sup> and Abhay N. Pasupathy<sup>1</sup>

The topology of Weyl semimetals requires the existence of unique surface states. Surface states have been visualized in spectroscopy measurements, but their connection to the topological character of the material remains largely unexplored. 1T'-MoTe<sub>2</sub> presents a unique opportunity to study this connection. This material undergoes a phase transition at 240 K that changes the structure from orthorhombic (putative Weyl semimetal) to monoclinic (trivial metal), while largely maintaining its bulk electronic structure. Here, we show from temperature-dependent quasiparticle interference measurements that this structural transition also acts as a topological switch for surface states in 1T'-MoTe<sub>2</sub>. At low temperature, we observe strong quasiparticle scattering, consistent with theoretical predictions and photoemission measurements for the surface states in this material. In contrast, measurements performed at room temperature show the complete absence of the scattering wavevectors associated with the trivial surface states. These distinct quasiparticle scattering behaviors show that 1T'-MoTe<sub>2</sub> is ideal for separating topological and trivial electronic phenomena via temperature-dependent measurements.

*npj Quantum Materials* (2018)3:2; doi:10.1038/s41535-017-0075-y

## INTRODUCTION

The Weyl fermion<sup>1</sup> is a massless chiral solution of the Dirac equation. Several solid-state materials whose crystal structures break time reversal or inversion symmetry have been predicted<sup>2–11</sup> and observed<sup>12–40</sup> to host quasiparticle excitations that mimic free Weyl fermions. In these Weyl semimetals, Weyl points exist as a touching between a hole and an electron pocket. While fundamental Weyl fermions are constrained by the Dirac equation to move at the speed of light, in the solid-state context the relationship between energy and momentum of the quasiparticles is determined by the material-specific band structure. In a type I Weyl semimetal, the hole and electron pockets which touch to form the Weyl points do not overlap in energy except at the Weyl points, leading to a band structure where quasiparticles exactly mimic fundamental Weyl fermions. In a type-II Weyl semimetal, however, the hole and electron pockets, which form the Weyl points, overlap over a range of energies. Type II Weyl fermions are only possible as a quasiparticle excitation in a system where Lorentz invariance is broken,<sup>6</sup> and thus are uniquely different from free Weyl fermions. Much recent activity has centered around the finding that at the surface of a Weyl semimetal, Weyl points are necessarily connected in pairs of opposite chirality by Fermi arc surface states, which form open contours on the Fermi surface.<sup>5,41</sup> Accordingly, most spectroscopic experiments have concentrated on observing the surface states in these materials. The majority

of these experiments have focused on type I Weyl semimetals,<sup>13–16,18–27,34,42</sup> with a smaller number of observations on type-II Weyl semimetals including MoTe<sub>2</sub><sup>30–32,35,36,40</sup> and its alloys with WTe<sub>2</sub>.<sup>33,37–39,43</sup> In spectroscopy measurements it is possible to conclusively prove the surface nature of electronic states; however, proving that the surface states are topologically protected arcs is a much more delicate task. An alternative way of studying Fermi surface properties is via transport. Many unique transport characteristics have been predicted for the Weyl band structures in general and the Fermi arc states in particular.<sup>44–51</sup> Transport experiments on Weyl semimetals have indeed seen several intriguing features;<sup>17,52–60</sup> however, the link to the Weyl band structure is often difficult to make. To clarify this connection, it would be ideal to use a system where Weyl behavior can be switched on and off using an experimentally tunable parameter like temperature, pressure or applied field.

One recently discovered type-II Weyl semimetal is MoTe<sub>2</sub>, a transition-metal dichalcogenide that exists as several different polytypes at high temperature.<sup>61,62</sup> At room temperature, the crystal structure is either hexagonal (2H, or  $\alpha$ -phase) or monoclinic (1T', or  $\beta$ -phase). When the monoclinic phase is cooled it undergoes a structural transition at 250 K to become orthorhombic, known as the Td phase.<sup>61,62</sup> In the Td phase, each Mo atom is at the center of a buckled Te octahedron, as seen in Fig. 1. The Td phase breaks inversion symmetry, and theoretical predictions of the electronic structure of this phase indicate

<sup>1</sup>Department of Physics, Columbia University, New York, NY 10027, USA; <sup>2</sup>Department of Applied Physics and Applied Mathematics, Columbia University, New York, NY 10027, USA; <sup>3</sup>Westlake Institute for Advanced Study, Hanzhou, China; <sup>4</sup>Department of Physics, Princeton University, Princeton, NJ 08520, USA; <sup>5</sup>Laboratory for Pohang Emergent Materials and Max Planck POSTECH Center for Complex Phase Materials, Max Planck POSTECH/Korea Research Initiative, Pohang 790-784, Korea; <sup>6</sup>Rutgers Center for Emergent Materials and Department of Physics and Astronomy, Rutgers University, Piscataway, NJ 08854, USA; <sup>7</sup>Department of Applied Physics and Applied Mathematics, Columbia University, New York, NY 10027, USA; <sup>8</sup>Synchrotron SOLEIL Orme des Merisiers, Saint Aubin BP 48, 91192 Gif Sur Yvette Cedex, France; <sup>9</sup>Laboratoire Pierre Aigrain, Ecole Normale Supérieure-PSL Research University, CNRS, Université Pierre et Marie Curie-Sorbonne Universités, Université Paris Diderot-Sorbonne Parice Cité, 24 rue Lhomond, 75231 Paris Cedex 05, France; <sup>10</sup>Donostia International Physics Center, P. Manuel de Lardizabal 4, 20018 Donostia-San Sebastián, Spain and <sup>11</sup>Sorbonne Universités, UPMC Univ Paris 06, UMR 7589, LPTHE, F-75005 Paris, France

Correspondence: Abhay N. Pasupathy (apn2108@columbia.edu)

Ayelet Notis Berger and Erick Andrade contributed equally to this work.

Received: 7 June 2017 Revised: 10 November 2017 Accepted: 18 December 2017

Published online: 16 January 2018

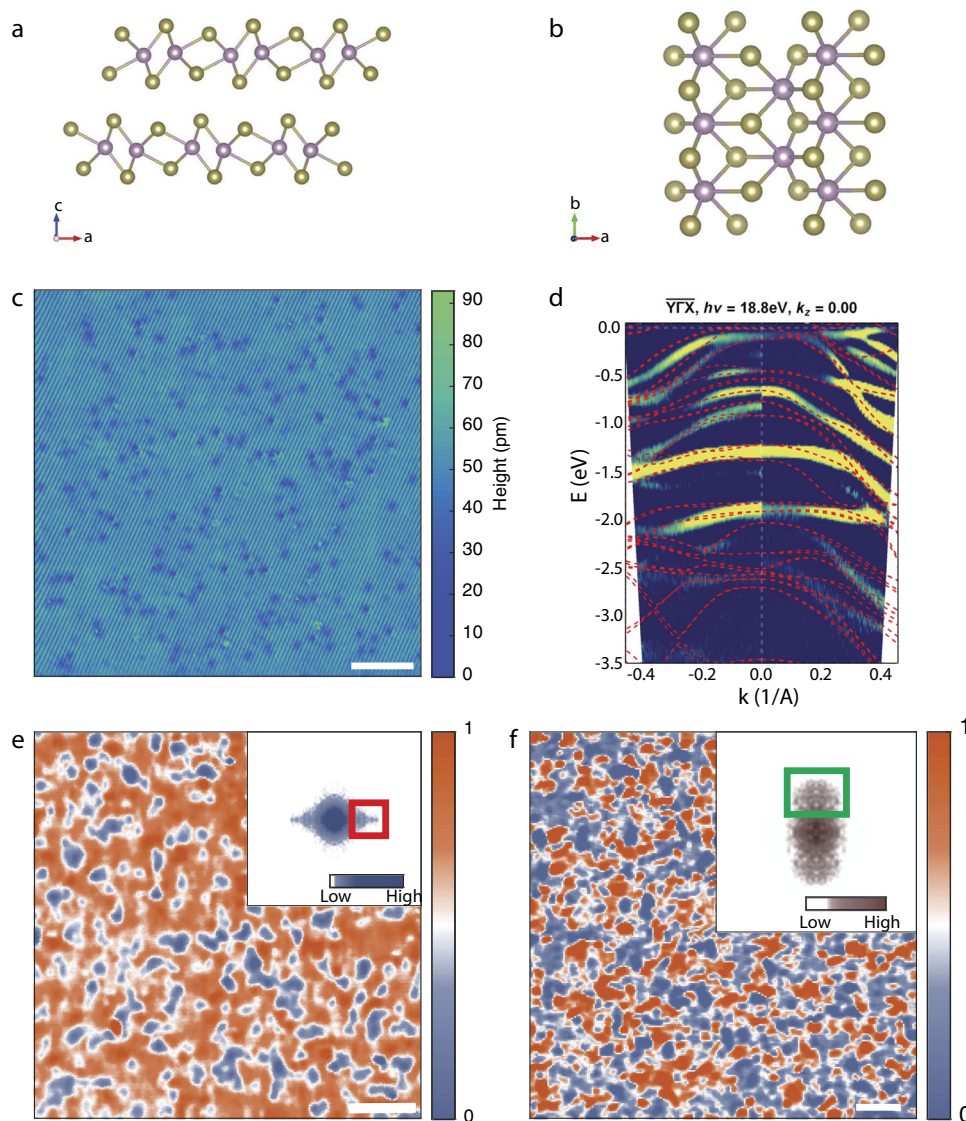


**Fig. 1** Td-MoTe<sub>2</sub> (a, b) Ball and Stick models showing projected views of Td-MoTe<sub>2</sub>. The Te atoms are represented in yellow, and the Mo atoms are in purple. c Constant-current STM topographic image of MoTe<sub>2</sub> ( $V = -200$  mV,  $I = -150$  pA,  $T = 6$  K). The rows seen run parallel to the  $b$ -axis of the crystal and come from the  $c$ -axis buckling in the Td crystal structure. d Two-dimensional cuts of the band structure along the high-symmetry directions X-Gamma-Y over a wide range of energy as measured by ARPES (2nd derivative applied) at  $T \sim 90$  K. The red dashed lines represent theoretical predictions of the bulk band structure. e, f Differential conductance ( $dI/dV$ ) map with insets showing Fourier transforms of the real-space maps. e shows a map at  $-35$  meV (normalization  $V = -300$  mV,  $I = -350$  pA,  $T = 6$  K). The Fourier transform inset shows wings aligned with the  $a$ -axis of the crystal (red box). f shows a map of a different area at  $50$  meV (normalization  $V = 200$  mV,  $I = 150$  pA,  $T = 6$  K). The Fourier transform inset shows a vertically dispersing feature aligned with the  $b$  crystal axis (green box). All scale bars shown in this figure represent  $10$  nm

that it is a topological type-II Weyl semimetal, although the number of Weyl points and the location of the associated Fermi arcs are very sensitive to the exact lattice parameters.<sup>7,8</sup> On the other hand, in the monoclinic 1T' phase, inversion symmetry is restored and the material is topologically trivial. Thus, the cooling or warming of a sample across the orthorhombic-monoclinic phase boundary offers a clean and simple way to compare the electronic properties in the topologically trivial and non-trivial phases. In this work, we demonstrate this switching behavior by visualizing changes in electronic structure across the temperature boundary. We supplement our experimental measurements with theoretical calculations and angle resolved photoemission spectroscopy (ARPES) measurements of the band structure.

## RESULTS

Our scanning tunneling microscopy (STM) and ARPES measurements are performed on crystals grown by the flux method (details in Methods) and quenched from high temperature to preserve the metastable 1T' phase at room temperature. Measurements are performed on in-situ cleaved crystals. STM topographic measurements taken over large areas (Fig. 1c) show clean, flat surfaces with several defects present at both the chalcogen and the metal sites. Figure 1d shows two-dimensional cuts of the band structure measured by ARPES along the cuts X-Gamma-Y over a wide range of energy. Our measurements are consistent with theoretical calculations and previous measurements<sup>30–32</sup> on similar crystals indicating that the samples are indeed in the Td phase.

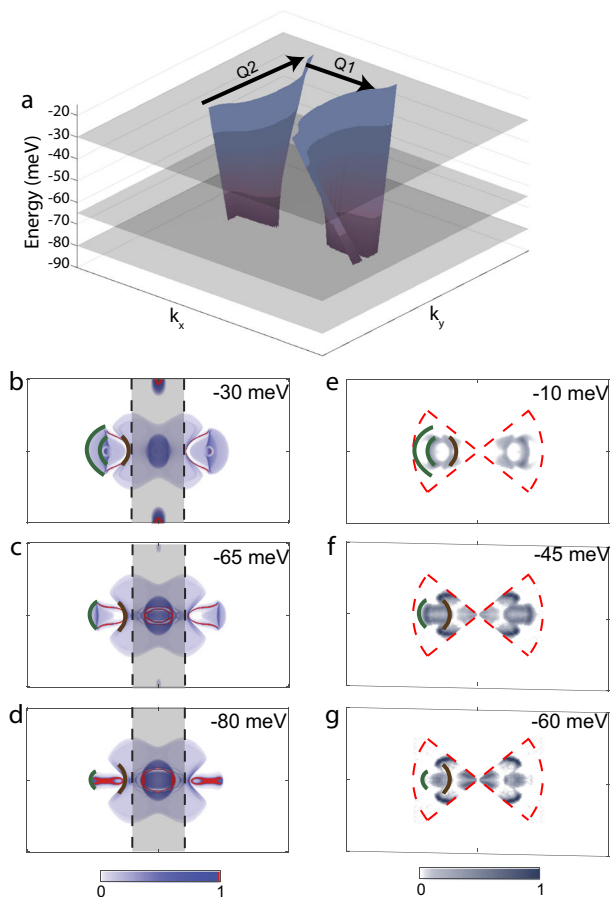


**Fig. 2** Surface bands in Td-MoTe<sub>2</sub>. **a** Dispersion associated with the surface bands. When the surface bands emerge at  $-80$  meV, their Fermi surfaces are long and narrow, and as the energy increases, the Fermi surfaces open up and become shorter. The surface band Fermi surfaces persist as easily distinguishable features until approximately  $-10$  meV. **b, c, d** Calculated constant energy contours, and **(e, f, g)** corresponding intensity maps (2nd derivative) measured through ARPES at various energies. The color map chosen for the calculated Fermi surface uses red for the most intense values, and blue for the rest of the band structure. This was deliberately chosen to highlight the fact that the surface states are much more intense than the bulk bands. The intensity corresponds to the density of states at a given momentum value, so the surface states by their two-dimensional nature are very sharp and concentrated in momentum space in comparison with the projected bulk states. The shaded gray rectangle shows where a mask was applied to exclude the more intense bulk bands in the center of the BZ from the thresholding. The red dashed lines in **(e, f, g)** denote the region over which ARPES measurements were performed. The ARPES measurements of the Fermi surface **(e, f, g)** show a surface band structure consistent with previous measurements. We outline the edges of the hole pocket in green and the edge of the electron pocket in brown to show how the evolution of the pockets matches between our ARPES data and calculated band structure. The data shown in panels **(e, f, g)** has been mirrored in  $k_x$  and  $k_y$  to show all quarters of the BZ. All of the band structure plots shown in this figure are cropped to the range  $k_x = (-0.5\pi/a, 0.5\pi/a)$  and  $k_y = (-0.5\pi/b, 0.5\pi/b)$

In scanning tunneling spectroscopy (STS) imaging measurements, real-space differential conductance images can be connected to the material band structure in the presence of scattering from crystal defects. Point defects in materials can act as elastic scattering centers, giving rise to quasiparticle interference (QPI) patterns that are located around each impurity. The wavevectors present in the interference pattern are related to the

momentum transfer provided by the defect in the scattering process. Shown in Fig. 1e, f are two real-space images that are obtained at  $-35$  and  $50$  mV, respectively. We find that the scattering from each individual defect in Td-MoTe<sub>2</sub> is weak, but the collective effect of all the scattering centers in the material causes clear modulations in the local density of states at each energy. This situation is reminiscent of similar experiments in other topological insulator materials.<sup>63</sup> The wavevectors present in the real-space image can be seen by taking a magnitude Fourier transform of the image, as shown in the inset to the real-space images in Fig. 1e, f (see Supplementary Information, section III, for more detailed spectroscopy maps). The QPI wavevectors we observe in Td-MoTe<sub>2</sub> have two distinctive features. First, as can be seen in the inset to Fig. 1e, we observe horizontal “wings” aligned with the a-axis of the crystal (red box, inset to Fig. 1e). Second, we observe a vertical stripe-like feature as seen in the inset of Fig. 1f (green box). This feature is aligned with the b-axis of the crystal. We describe the evolution of the intensity and wavevectors of the wings and the vertical stripes in detail below.

Our experimental results for the observed wavevectors from QPI can be compared to predictions based on theoretical calculations of the surface electronic structure. Our density-functional theory (DFT) calculations<sup>7</sup> using lattice parameters from x-ray diffraction at 100 K show four Weyl points at  $k = (0.1011, 0.0503, 0)$  and points related by the reflections  $M_{x,y}$ . Each pair of these Weyl points located at the same value of  $k_x$  is necessarily connected by Fermi arc surface states. In addition to these arcs, trivial surface states also exist in the same region in momentum space. We can calculate the surface band structure of the material at each energy either by projecting the full DFT calculation onto the surface, or from a tight-binding model that is constructed from DFT calculations (see methods). The computed surface band structure at three energies is shown in Fig. 2b–d. A number of bulk and surface bands are seen in these calculations. Since the surface states are truly two-dimensional, they can be easily picked out from the other contributions to the surface band structure by a simple process of thresholding the surface spectral density, as illustrated in Fig. 2b–d. The color map chosen uses shades of blue, with only the most intense values colored red. The surface states contrast sharply with their surrounding bulk bands located near the same wavevectors, so this color map easily identifies the surface states based on intensity. The identification of the surface states by this procedure allows us to track the evolution of these states in energy, as shown in Fig. 2a. We see that the surface bands are fairly localized in energy—they first appear around  $-80$  meV, then lose intensity and hybridize strongly with the bulk bands above  $-10$  meV. The evolution of hole and electron pockets (highlighted with brown and green lines) matches well with that found in measurements from ARPES, as shown in Fig. 2e–g. Our ARPES results are consistent with previous measurements<sup>30–32</sup> of the same material. The Weyl points themselves are not visualized in the data since they occur above the Fermi level.<sup>7</sup>

We note that calculations using a slightly different lattice constant ( $\sim 1\%$ )<sup>8</sup> produce different results for the surface state band structure. In our calculations,<sup>7</sup> there is one Weyl point in each quadrant of the BZ, located at  $(\pm 0.1011a^*, \pm 0.0503b^*, 0)$ . The large surface state connects the Weyl points across the  $k_y$  axis and is a topological Fermi arc. In the other calculation,<sup>8</sup> there are two Weyl points in each quadrant of the BZ at  $(\pm 0.1024a^*, \pm 0.0128b^*, 0)$  and  $(0.1001a^*, 0.0530b^*, 0)$ . The Fermi arcs are much smaller in extent and connect the Weyl points located within each quadrant. A large, singly degenerate surface state is seen in this calculation as well, although it is topologically trivial in this calculation. The origin of this large surface state is currently not understood theoretically—the fact that it is single degenerate is quite unusual, since its Rashba partner seems to be missing in the surface bands.<sup>35</sup> While the topological properties of the surface bands are quite different in the two calculations, the actual extent

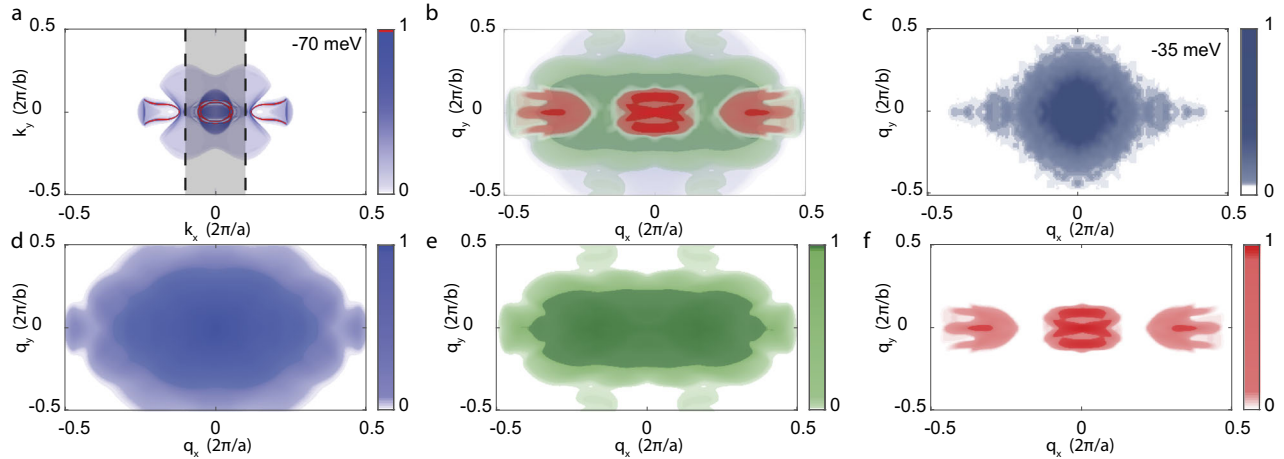


**Fig. 3** Demonstration of the procedure used to separate QPI from bulk, surface, and joint states. **a** shows the Fermi surface at  $-70$  meV. Because the Fermi arcs sharply contrast with the bulk states, they are easily separated from the rest of the band structure through intensity thresholding. The gray rectangle shows where a mask is applied to exclude the more intense bulk bands in the center from the threshold. **b** shows all three QPI components overlaid, with bulk shown in blue, joint shown in green, and surface shown in red. **c** shows the Fourier transform of a differential conductance map at  $-35$  meV, cropped to the first BZ for comparison to the calculated QPI. The horizontal wing feature matches with the QPI calculated from the Fermi arc surface states. **d** shows in blue the QPI coming from the bulk states only, with the Fermi arcs removed. **e** shows the joint QPI which comes from scattering between bulk and surface states. **f** shows the QPI coming only from the Fermi arc surface states

and dispersion of the surface bands themselves are very similar. We will comment further on the difference below, but we will proceed by comparing STM experiments to the calculations from Wang et al.<sup>7</sup>

Using our theoretically calculated band structure, we can now calculate the expected scattering wavevectors in a QPI experiment. An elastic scattering event from a defect results in a change in momentum  $q$  of a quasiparticle incident on it. Real-space interference patterns and their Fourier transforms will show intensity only at values of  $q$  allowed by the band structure at each energy.<sup>64–66</sup> Additional selection rules that govern the relative intensities for different  $q$  can exist due to crystal and time-reversal symmetry conservation laws,<sup>63</sup> structure of the scattering potential,<sup>66,67</sup> or matrix elements. In our experiments, we consider the impurities giving rise to scattering processes to be largely non-magnetic, as observed for other transition-metal dichalcogenides.<sup>66</sup> To compute the expected QPI pattern at every energy, we calculate the spin-conserved scattering probability

$$J_s(q) = \frac{1}{2} \sum_k \sum_{i=0,1,2,3} \rho_i(k) \rho_i(k+q) \quad (1)$$

where  $\rho_0(k)$  stands for charge densities, and  $\rho_i(k)$  ( $i = 1, 2, 3$ ) stands for spin densities along three orthogonal orientations [see Methods].

While the experimental QPI occurs at allowed values of  $q$  from the theory, only a subset of the theoretically allowed values is actually observed in experiment. It is, therefore, worth understanding the sources within theory of the features that are seen in experiment. In general, the surface band structure has a part that comes from the surface states (red band in Fig. 3a), and a remainder that comes from the projections of various bulk bands. A scattering process can, therefore, take place between bulk bands alone, from a bulk to a surface band, or between the surface bands alone. We decompose the theoretical band structure (3a) into surface and bulk bands to calculate the three separate QPI components, shown in Fig. 3d–f. By comparing each of these separately with the experimental QPI in Fig. 3c, we see that the most distinctive feature of the experimental QPI (the “wings” denoted by the circled region) is seen prominently in the surface-surface scattering as well as (to a lesser extent) in the surface-bulk scattering. On the other hand, the bulk-bulk

scattering does not show any particular features at this intensity, and indeed several of the features seen in the bulk scattering do not exist in the experiment. Thus, on the basis of the match between theory and experiment, we can identify the “wings” as being associated with surface state scattering.

Next, we consider the dispersion of the QPI features with energy. Shown in Fig. 4a–f are the expected QPI from theory, color-coded as before to distinguish the various contributions to scattering. Inspection of this energy evolution shows two distinctive features associated with the surface state scattering, coming from inter-arc and intra-arc scattering, respectively. The inter-arc scattering that has already been discussed above leads to the “wings” along the  $k_x$  direction that disperse along the  $y$  direction with increasing energy, as a consequence of similar dispersion in the surface bands themselves. The second prominent feature observed in the surface state scattering is intra-arc scattering, which is seen for small momentum transfers. At the lowest energies where the arcs are observed ( $-80$  mV), the intra-arc scattering is difficult to distinguish from strong bulk scattering that is present at the same wavevectors (Fig. 4m). However, as the energy increases (going from Fig. 4a–f), the intra-arc scattering disperses outwards along  $k_y$ , while at the same time the amount of bulk scattering present at these wavevectors diminishes. Since the inter-arc and intra-arc scatterings appear at very different wavevectors, we perform two separate imaging experiments with different real-space size scales to see the two scatterings clearly. An additional complication in the comparison between theory and experiment is the presence of Fermi level shifts in the sample as a function of spatial position or time. Such shifts, which have been documented to occur because of surface doping,<sup>30,68</sup> sample aging,<sup>69</sup> chemical inhomogeneity<sup>70</sup> or non-stoichiometry<sup>57</sup> in both topological insulators<sup>68–70</sup> and semimetals,<sup>30,57</sup> imply that an energy shift has to be applied to the experimental data before comparison with theory. Shown in Fig. 4a–f and Fig. 4g–l are two sets of experimental data that are acquired to make comparison with the inter-arc and intra-arc scattering features, respectively, (see Supplementary Information, section IV, for details of energy alignment between the two data sets). Imaging performed over a larger real-space area (Fig. 4g–l) reveals the intra-arc scattering wavevectors. While the inter-arc scattering is also observed weakly at this real-space resolution (see Supplementary Sections III, IV for

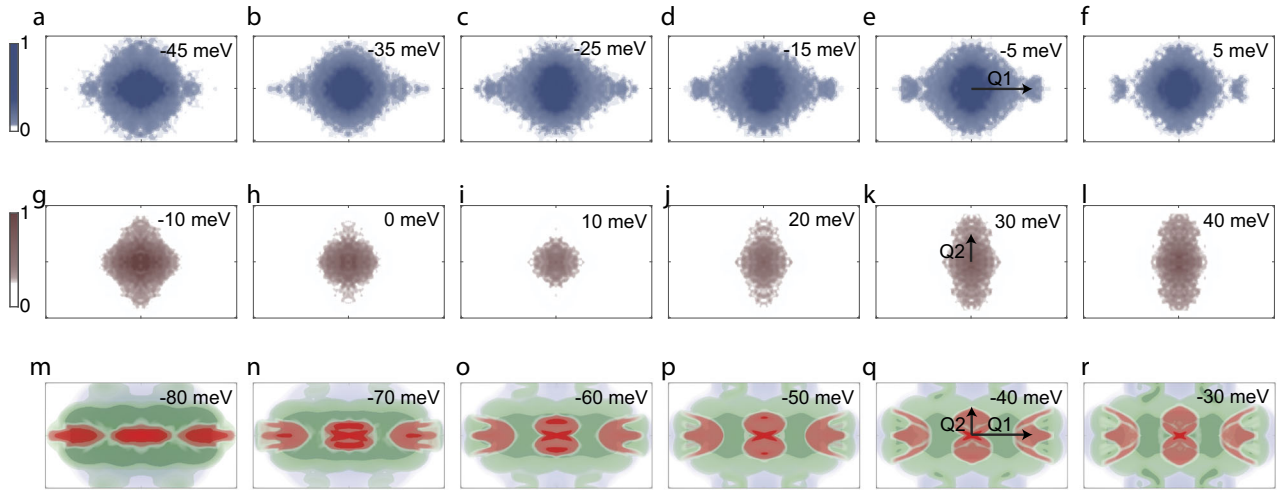


**Fig. 4** Comparison of QPI from differential conductance maps and calculated QPI. **a–f**  $dl/dV$  map optimized for showing the horizontal dispersion. **g–l**  $dl/dV$  map optimized for showing the vertical dispersion. **m–r** QPI calculated from tight-binding data using the procedure shown in Fig. 3. Blue represents QPI from bulk states, green is QPI from scattering between bulk and surface states, and red is QPI from surface states. All QPI images are cropped to the range  $q_x = (-0.5\pi/a, 0.5\pi/a)$  and  $q_y = (-0.5\pi/b, 0.5\pi/b)$ , and aligned in energy as shown in Supplementary

more details), imaging performed on a smaller area (Fig. 4a–f) reveals the large wavevector, inter-arc scattering (“wings”) more clearly. We see from these data sets that the experimental dispersion of the QPI features matches reasonably well with both the intra-arc and inter-arc scatterings.

While our low-temperature STS measurements are in good agreement with our surface state calculations, we have explained earlier that the calculations themselves are extremely sensitive to the lattice parameters used. Theoretically, the large surface state from which we see QPI can be rendered topological or not by changing the small  $k_y$  parts of the band structure—however, these changes are very hard to detect in QPI or other spectroscopic experiments due to limited experimental resolution. Thus, detecting the surface states at low temperature alone is not rigorous enough to claim agreement with the theoretical Fermi arcs. In our experiments, we are able to use the temperature-driven phase transition to gain crucial additional insight into the topological character of 1T'-MoTe<sub>2</sub>. The orthorhombic-monoclinic structural transition involves a small ( $\sim 3$  degrees) distortion of the  $c$ -axis stacking while otherwise leaving the structure intact. As a consequence, the bulk band structure is only very slightly changed between the two phases. This is shown in Fig. 5a, b, which are the surface-projected band structures at  $-60$  meV calculated by tight binding for both phases. We can see that the overall bulk band structure is very similar for both phases. However, an important consequence of the phase transition is that inversion symmetry is recovered in the monoclinic phase, implying that the high-temperature phase does not have Weyl points with topologically protected Fermi arc surface states. Topologically trivial surface states can still exist in the material, and a close examination of Fig. 5b interestingly shows that such a trivial surface state does exist at high temperature. The surface states at low and high temperature are highlighted on the  $k_x < 0$  side of Fig. 5a, b in brown (further details of the dispersion of the band structure in both phases is provided in the supporting information, section VIII).

We can calculate the expected QPI based on our surface-projected tight-binding band structure at high temperature. Since we see experimental features primarily corresponding to the surface state scattering at low temperature, we concentrate on comparing the scattering expected from the surface states when they are non-overlapping with the bulk bands at the same energy. Shown in Fig. 5c, d are the expected QPI from the surface states in

both phases at  $-60$  meV, shown on the same intensity color scale. We note that in this calculation we have included a thermal broadening of 300 K to the band structure of both phases, to fairly compare the expected QPI from both phases to room temperature experiments. We see that the Weyl semimetal phase shows a strong signature of the “wings” that we have previously described, and that these “wings” are clearly present even after thermal broadening to 300 K. On the other hand, the monoclinic phase band structure shows very weak structure at the wavevectors of the wings. This happens in our calculations because the length of the surface state that is non-overlapping with the bulk states is much shorter in the trivial phase when compared to the semimetal phases, and consequently its intensity in the QPI pattern is much weaker.

In order to visualize the difference between the low and high-temperature surface state structure, we proceed to perform STM/STS imaging at room temperature. Such experiments are in general technically challenging, and to avoid problems of sample contamination the experiments are performed on a freshly cleaved crystal with the microscope maintained at room temperature. We are successfully able to obtain atomic resolution imaging and spectroscopy (see Supplementary Information, section V, for real-space images and detailed spectroscopy results). To verify the capability of our instrument at room temperature, we also perform successful imaging experiments on the well-known Shockley surface state of gold (111) (see Supplementary Information, section VI for details of these measurements). In the case of 1T'-MoTe<sub>2</sub>, we show in Fig. 5f a Fourier transform in the same energy range where QPI is observed at low temperature. It is evident from the data that the high-temperature QPI shows no evidence for surface state dispersion at the wavevectors where it is observed at low temperature. We have already discussed the role of thermal broadening from the theoretical perspective above. We can also ask the purely experimental question—given the observed low-temperature QPI patterns in experiment shown in Figs. 1, 3, and 4, what do we expect room temperature thermal broadening to do to these QPI patterns? We address this in two different ways. First, we perform a simple test to simulate thermal broadening at low temperature. The QPI signal is the Fourier transform of the experimentally measured differential conductance. The differential conductance is measured with a lock-in amplifier by applying an AC voltage and measuring the AC current response, and the overall broadening of the experimental

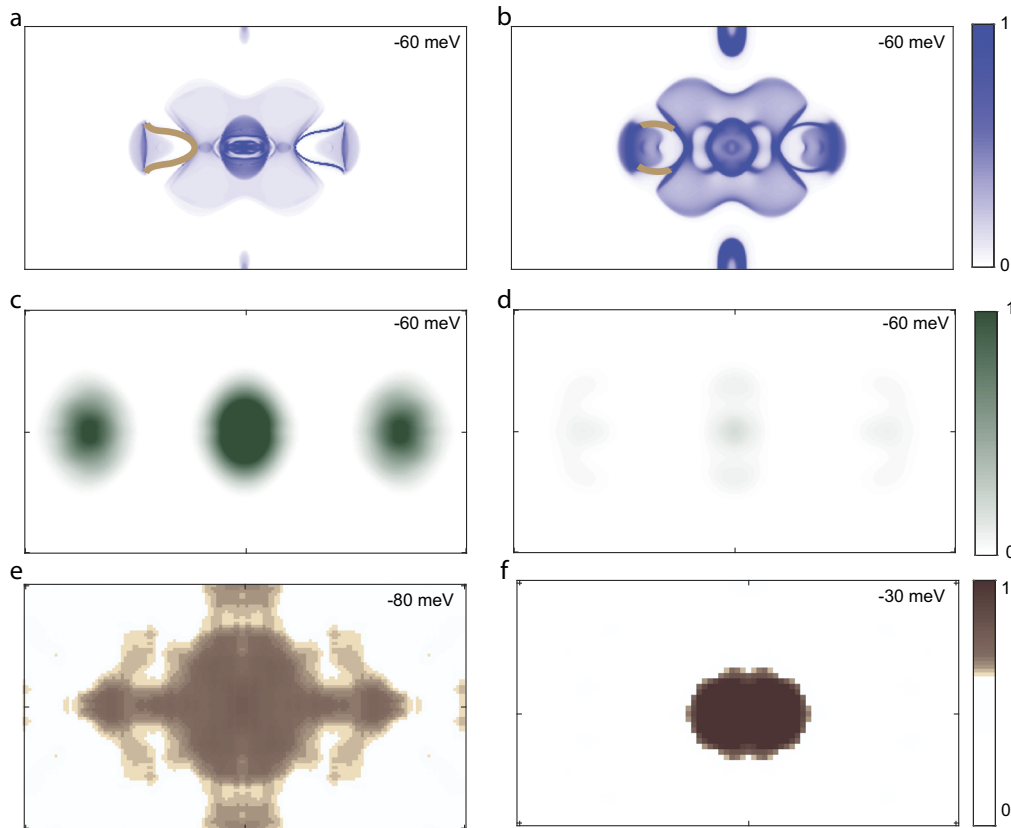


**Fig. 5** Comparison of the high-temperature and low-temperature phases. **a, b** The Fermi surfaces, calculated by tight binding, of the orthorhombic,  $T_d$  phase at low temperature (**a**), and the monoclinic  $1T'$  phase at high temperature. Surface states are present in both phases, highlighted on the left half of the Brillouin zone with brown contours. **c, d** QPI from tight-binding surface states (only the parts that do not overlap with bulk bands) that have been thermally broadened to  $T = 300$  K, as described in Supplementary Section VI, for the orthorhombic (**c**), and monoclinic (**d**) phases. Both phases show a horizontal wing feature in the QPI, but the intensity is much lower in the monoclinic phase, mostly due to overlap of the surface and bulk states. **e** Fourier transform of differential conductance map taken at low temperature with a 30 meV bias oscillation to simulate room temperature thermal broadening (see text). The horizontal wing feature is still visible in the QPI, even in the presence of energy broadening. **f** Fourier transform of differential conductance map taken at room temperature. No features are seen in the QPI. All of the plots shown are cropped to the first BZ, to the range  $k_x$  or  $q_x = (-0.5\pi/a, 0.5\pi/a)$  and  $k_y$  or  $q_y = (-0.5\pi/b, 0.5\pi/b)$

spectrum is given by adding in quadrature the temperature broadening and the broadening due to the AC voltage. While we typically use an AC voltage that is comparable to the real sample temperature, we intentionally simulated the effect of high temperature by performing a low-temperature measurement with a large AC voltage (RMS value of 30 meV), similar to room temperature. QPI results of this experiment at  $-80$  meV are shown in Fig. 5e (see Supplementary Information, section VII, for additional energies and more details on simulating thermal effects). As can be seen, we can still clearly see the “wing” features in the QPI along with additional features that are introduced after the broadening of the spectrum. A second test is to directly apply an energy broadening corresponding to room temperature to the measured low-temperature QPI patterns. These calculations, described in Supplementary Information, section VII, also confirm that we expect the “wing” features to survive room temperature broadening. Both of these tests clearly show that the absence of QPI at high temperature is not an experimental artifact, but is rather a consequence of the difference in electronic properties of the sample at high temperature.

## DISCUSSION

Our observation of the absence of the high-temperature QPI at the wavevectors corresponding to the “wings” is reasonably consistent with our theoretical calculations, which show a heavy

suppression of this feature in the trivial phase (Fig. 5d and Supplementary Information, section V). The complete absence of the feature at high temperature rather than a suppression of the intensity could additionally arise from a loss of topological protection of the surface state. Thus, at low temperature, the large surface state is topologically protected against the effects of disorder—at least at small momentum scattering, while no such topological protection—beyond weak antilocalization—should exist at high temperature. This would be compatible with a scenario where the surface states at high temperature are not observed due to disorder (as has been observed in other metallic surface states,<sup>71</sup>) while they survive at low temperature due to the topological protection. Future experiments on samples with varying levels of disorder can help shed light on whether surface state localization is significant at high temperature. We also note that this scenario where topological protection is responsible for explaining the low-temperature QPI is more compatible with the four Weyl point calculation rather than the eight Weyl point calculation (where the large surface state is trivial at both low and high temperature). Regardless of the details of the high-temperature surface state, this type of temperature-driven phase transition where the electronic structure is largely preserved but the topological character is changed presents a unique opportunity to isolate the effect of topological Fermi arcs on the properties of Weyl semimetals. By alloying (or by applying physical knobs such as strain or pressure) one could imagine

pushing the phase boundary down to low temperature, where topological phenomena can be turned on and off by small changes in temperature. This offers the potential of isolating topological phenomena from non-topological, a major challenge in current spectroscopic and transport experiments.

## METHODS

Samples were grown by flux method. MoTe<sub>2</sub> powder was well mixed with sodium chloride (NaCl, molar ratio is about 1:7) and put in an alumina tube. This alumina tube was then sealed in a vacuumed quartz tube of pressure 0.18 Pa. Then, the glass tube was put in a Muffle furnace and heated at 1100 °C for 12 h, followed by cooling to 900 °C at a rate of 0.5 °C/h. The quartz tube was then water quenched to room temperature to achieve the 1T phase MoTe<sub>2</sub> crystals. Electrical resistivity measurement was carried out using a standard 4-probe technique in a physical property measurement system (Quantum Design, 9T-PPMS).

Our DFT calculations are generally based on the Vienna ab initio simulation package,<sup>72</sup> and use the core-electron projector augmented wave basis sets<sup>73</sup> with the generalized-gradient method.<sup>74</sup> Spin-orbital coupling is included self-consistently. The cutoff energy for wave-function expansion is 300 eV. Experimental lattice parameters are used throughout our calculations. To reduce the computation load in certain cases (e.g., in the comparison of the low-temperature and the high-temperature structures of MoTe<sub>2</sub>), we construct tight-binding models by using the maximally localized Wannier function approach<sup>75</sup> and by keeping only the degrees of freedom corresponding to the Mo 4d orbitals and the Te 5p orbitals.

To obtain the spectral and spin densities on the surface of MoTe<sub>2</sub> from DFT calculations, we use a slab model of four surface unit cells (with two atomic layers per unit cell) in thickness, and with a (001) surface orientation. We use in-plane k-point grids of size 14 × 8 for the charge self-consistent calculations, and of size 1000 × 400 for the Fermi surface calculations. To obtain the surface spectral and spin densities from tight-binding models, we use the algorithm by Lopez Sancho et al.<sup>76</sup> to calculate the surface Green functions with 400 × 400 in-plane k-point grids.

The calculated spectral density is defined by  $\rho_0(k, E) = \text{Tr}(A(k, E))$ , and the spin densities are defined by  $\rho_i(k, E) = \text{Tr}(\sigma_i A(k, E))$ , with  $A(k, E)$  the matrix spectral function and  $\sigma_i$  the Pauli matrices for spin. The matrix spectral function  $A(k, E)$  can be constructed from the Bloch eigenstates  $\{\psi_n(k)\}$  ( $n$  is the band index), obtained from the DFT calculations, for a specific energy  $E$ , by taking its standard definition

$$A(k, E) = \sum_n -\frac{1}{\pi} \text{Im} \left( \frac{1}{E - E_n(k) + i\eta} \right) \psi_n(k) \psi_n^\dagger(k) \quad (2)$$

Here  $E_n(k)$  is the energy of the  $n$ -th Bloch band, the eigenstate  $\psi_n(k)$  is a column vector, and  $\eta$  is a small number typically of value 2 meV. Alternatively,  $A(k, E)$  can be obtained from the retarded surface Green functions  $G^R(k, E)$ , as in the case of tight-binding calculations, with an equivalent definition:

$$A(k, E) = \frac{i}{2\pi} \left[ G^R(k, E) - G^R(k, E)^\dagger \right] \quad (3)$$

All  $\rho_0$  and  $\rho_{1,2,3}$  can be projected to specific layers by keeping  $A(k, E)$  only for the appropriate atoms.

All angle resolved photoemission measurements were performed at the ANTARES [78] beamline located at the SOLEIL synchrotron, Gif sur Yvette, France. The beam spot size was 120 μm. The angular and energy resolution of the beamline at a photon energy of 18.8 eV are 0.2° and 10 meV, respectively. Linear polarized light was used. All data shown here were obtained at 90 K.

## Data availability

All relevant data is available upon request from the corresponding author.

## ACKNOWLEDGEMENTS

This work is supported by the National Science Foundation (NSF) via the Materials Research Science and Engineering Center at Columbia University (grant DMR 1420634), by grant DMR-1610110 (A.N.) and by the Office of Naval Research grant number N00014-14-1-0501 (E.A.). Equipment support is provided by the Air Force Office of Scientific Research (grant number FA9550-16-1-0601) and FA9550-16-1-0031, J.P.). B.A.B. acknowledges support from NSF EAGER Award NOA-AWD1004957,

ONR-N00014-14-1-0330, ARO MURI W911NF-12-1-0461, NSF-MRSEC DMR-1420541. Z. J.W.'s work was supported by Department of Energy de-sc0016239, Simons Investigator Award, Packard Foundation and Schmidt Fund for Innovative Research. The work at Postech was supported by the Max Planck POSTECH/KOREA Research Initiative Program through National Foundation of Korea (NRF) funded by the Ministry of Science, ICT and Future Planning (No. 2016K1A4A4A01922028). The work at Rutgers was funded by the Gordon and Betty Moore Foundation's EPIOS Initiative through Grant GBMF4413 to the Rutgers Center for Emergent Materials. N.Z. acknowledges support by the NSF MRSEC program through Columbia in the Center for Precision Assembly of Superstratic and Superatomic Solids (DMR-1420634). M.C.A., J.A., and C.C. acknowledge Synchrotron SOLEIL, which is supported by the Center National de la Recherche Scientifique (CNRS) and the Commissariat à l'Energie Atomique et aux Energies Alternatives (CEA), France.

## AUTHOR CONTRIBUTIONS

A.N.B. and E.A. performed STM experiments and analysis. J.L., Z.W., and B.A.B. performed theoretical analysis. N.Z., J.A., C.C., and M.C.A. performed ARPES experiments and analysis. L.Z. and J.K. grew single crystals. B.A.B., S.-W.C., and A.N.P. advised. A.N.P. is the guarantor of the research. A.N.B. and A.P.N. co-wrote the paper, and all authors contributed to the discussion and preparation of the manuscript.

## ADDITIONAL INFORMATION

**Supplementary information** accompanies the paper on the *npj Quantum Materials* website (<https://doi.org/10.1038/s41535-017-0075-y>).

**Competing interests:** The authors declare no competing financial interests.

**Publisher's note:** Springer Nature remains neutral with regard to jurisdictional claims in published maps and institutional affiliations.

## REFERENCES

- Weyl, H. Gravitation and the electron. *Proc. Natl. Acad. Sci. USA* **15**, 323–334 (1929).
- Huang, S. M. et al. A Weyl Fermion semimetal with surface Fermi arcs in the transition metal monophosphide TaAs class. *Nat. Commun.* **6**, 7373 (2015).
- Weng, H. M., Fang, C., Fang, Z., Bernevig, B. A. & Dai, X. Weyl Semimetal phase in noncentrosymmetric transition-metal monophosphides. *Phys. Rev. X* **5**, 011029 (2015).
- Burkov, A. A. & Balents, L. Weyl semimetal in a topological insulator multilayer. *Phys. Rev. Lett.* **107**, 127205 (2011).
- Wan, X., Turner, A. M., Vishwanath, A. & Savrasov, S. Y. Topological semimetal and Fermi-arc surface states in the electronic structure of pyrochlore iridates. *Phys. Rev. B* **83**, 205101 (2011).
- Soluyanov, A. A. et al. Type-II Weyl semimetals. *Nature* **527**, 495–498 (2015).
- Wang, Z. et al. MoTe<sub>2</sub>: A type-II Weyl topological metal. *Phys. Rev. Lett.* **117**, 056805 (2016).
- Sun, Y., Wu, S. C., Ali, M. N., Felsner, C. & Yan, B. H. Prediction of Weyl semimetal in orthorhombic MoTe<sub>2</sub>. *Phys. Rev. B* **92**, 161107 (2015).
- Chang, T. R. et al. Prediction of an arc-tunable Weyl Fermion metallic state in MoxW1-xTe2. *Nat. Commun.* **7**, 10639 (2016).
- Singh, B. et al. Topological electronic structure and Weyl semimetal in the TlBiSe2 class of semiconductors. *Phys. Rev. B* **86**, 115208 (2012).
- Huang, S. M. et al. New type of Weyl semimetal with quadratic double Weyl fermions. *Proc. Natl. Acad. Sci. USA* **113**, 1180–1185 (2016).
- Arnold, F. et al. Negative magnetoresistance without well-defined chirality in the Weyl semimetal TaP. *Nat. Commun.* **7**, 11615 (2016).
- Belopolski, I. et al. Observation of surface states derived from topological Fermi arcs in the Weyl semimetal NbP. Preprint at <https://arxiv.org/abs/1509.07465> (2015).
- Liu, Z. K. et al. Evolution of the Fermi surface of Weyl semimetals in the transition metal pnictide family. *Nat. Mater.* **15**, 27–32 (2016).
- Lv, B. Q. et al. Experimental discovery of Weyl semimetal TaAs. *Phys. Rev. X* **5**, 031013 (2015).
- Lv, B. Q. et al. Observation of Weyl nodes in TaAs. *Nat. Phys.* **11**, 724–727 (2015).
- Shekhar, C. et al. Extremely large magnetoresistance and ultrahigh mobility in the topological Weyl semimetal candidate NbP. *Nat. Phys.* **11**, 645–650 (2015).
- Xu, N. et al. Observation of Weyl nodes and Fermi arcs in tantalum phosphide. *Nat. Commun.* **7**, 11006 (2016).
- Xu, S.-Y. et al. Experimental discovery of a topological Weyl semimetal state in TaP. *Sci. Adv.* **1**, 1501092 (2015).

20. Xu, S. Y. et al. Discovery of a Weyl fermion state with Fermi arcs in niobium arsenide. *Nat. Phys.* **11**, 748–755 (2015).
21. Xu, S. Y. et al. Discovery of a Weyl fermion semimetal and topological Fermi arcs. *Science* **349**, 613–617 (2015).
22. Yang, L. X. et al. Weyl semimetal phase in the non-centrosymmetric compound TaAs. *Nat. Phys.* **11**, 728–733 (2015).
23. Zheng, H. et al. Atomic-scale visualization of quantum interference on a Weyl semimetal surface by scanning tunneling microscopy. *ACS Nano* **10**, 1378–1385 (2016).
24. Liu, Z. K. et al. Discovery of a three-dimensional topological Dirac semimetal, Na<sub>3</sub>Bi. *Science* **343**, 864–867 (2014).
25. Borisenko, S. et al. Experimental realization of a three-dimensional Dirac semimetal. *Phys. Rev. Lett.* **113**, 027603 (2014).
26. Neupane, M. et al. Observation of a three-dimensional topological Dirac semimetal phase in high-mobility Cd<sub>3</sub>As<sub>2</sub>. *Nat. Commun.* **5**, 3786 (2014).
27. Jeon, S. et al. Landau quantization and quasiparticle interference in the three-dimensional Dirac semimetal Cd<sub>3</sub>As<sub>2</sub>. *Nat. Mater.* **13**, 851–856 (2014).
28. Xu, G., Weng, H., Wang, Z., Dai, X. & Fang, Z. Chern semimetal and the quantized anomalous Hall effect in HgCr<sub>2</sub>Se<sub>4</sub>. *Phys. Rev. Lett.* **107**, 186806 (2011).
29. Fang, C., Gilbert, M. J., Dai, X. & Bernevig, B. A. Multi-Weyl topological semimetals stabilized by point group symmetry. *Phys. Rev. Lett.* **108**, 266802 (2012).
30. Deng, K. et al. Experimental observation of topological Fermi arcs in type-II Weyl semimetal MoTe<sub>2</sub>. *Nat. Phys.* **12**, 1105–1110 (2016).
31. Huang, L. et al. Spectroscopic evidence for a type II Weyl semimetallic state in MoTe<sub>2</sub>. *Nat. Mater.* **15**, 1155–1160 (2016).
32. Tamai, A. et al. Fermi arcs and their topological character in the candidate type-II Weyl semimetal MoTe<sub>2</sub>. *Phys. Rev. X* **6**, 031021 (2016).
33. Belopolski, I. et al. Discovery of a new type of topological Weyl fermion semimetal state in Mo<sub>x</sub>W<sub>1-x</sub>Te<sub>2</sub>. *Nat. Commun.* **7**, 13643 (2016).
34. Inoue, H. et al. Quasiparticle interference of the Fermi arcs and surface-bulk connectivity of a Weyl semimetal. *Science* **351**, 1184–1187 (2016).
35. Jiang, J. et al. Signature of type-II Weyl semimetal phase in MoTe<sub>2</sub>. *Nat. Commun.* **8**, 13973 (2017).
36. Liang, A. et al. Electronic evidence for type II Weyl semimetal state in MoTe<sub>2</sub>. Preprint at <https://arxiv.org/abs/1604.01706> (2016).
37. Wang, C. et al. Observation of Fermi arc and its connection with bulk states in the candidate type-II Weyl semimetal WTe<sub>2</sub>. *Phys. Rev. B* **94**, 241119 (2016).
38. Wu, Y. et al. Observation of Fermi arcs in the type-II Weyl semimetal candidate WTe<sub>2</sub>. *Phys. Rev. B* **94**, 121113 (2016).
39. Zheng, H. et al. Atomic-scale visualization of quasiparticle interference on a type-II Weyl semimetal surface. *Phys. Rev. Lett.* **117**, 266804 (2016).
40. Xu, N. et al. Discovery of Weyl semimetal state violating Lorentz invariance in MoTe<sub>2</sub>. Preprint at <https://arxiv.org/abs/1604.02116> (2016).
41. Silaev, M. A. & Volovik, G. E. Topological Fermi arcs in superfluid <sup>3</sup>He. *Phys. Rev. B* **86**, 214511 (2012).
42. Lu, L. et al. Experimental observation of Weyl points. *Science* **349**, 622–624 (2015).
43. Bruno, F. Y. et al. Observation of large topologically trivial Fermi arcs in the candidate type-II Weyl semimetal WTe<sub>2</sub>. *Phys. Rev. B* **94**, 121112 (2016).
44. Zyuzin, A. A. & Burkov, A. A. Topological response in Weyl semimetals and the chiral anomaly. *Phys. Rev. B* **86**, 115133 (2012).
45. Nielsen, H. B. & Ninomiya, M. The Adler-Bell-Jackiw anomaly and Weyl fermions in a crystal. *Phys. Lett. B* **130**, 389–396 (1983).
46. Son, D. T. & Spivak, B. Z. Chiral anomaly and classical negative magnetoresistance of Weyl metals. *Phys. Rev. B* **88**, 104412 (2013).
47. Burkov, A. A. Negative longitudinal magnetoresistance in Dirac and Weyl metals. *Phys. Rev. B* **91**, 245157 (2015).
48. Baum, Y., Berg, E., Parameswaran, S. A. & Stern, A. Current at a distance and resonant transparency in Weyl semimetals. *Phys. Rev. X* **5**, 041046 (2015).
49. Parameswaran, S. A., Grover, T., Abanin, D. A., Pesin, D. A. & Vishwanath, A. Probing the chiral anomaly with nonlocal transport in three-dimensional topological semimetals. *Phys. Rev. X* **4**, 031035 (2014).
50. Potter, A. C., Kimchi, I. & Vishwanath, A. Quantum oscillations from surface Fermi arcs in Weyl and Dirac semimetals. *Nat. Commun.* **5**, 5161 (2014).
51. Sun, Y., Zhang, Y., Felsner, C. & Yan, B. Strong intrinsic spin Hall effect in the TaAs family of Weyl semimetals. *Phys. Rev. Lett.* **117**, 146403 (2016).
52. Lv, Y.-Y. et al. Experimental observation of anisotropic Adler-Bell-Jackiw anomaly in type-II Weyl semimetal WTe<sub>1.98</sub> crystals at the quasiclassical regime. *Phys. Rev. Lett.* **118**, 096603 (2017).
53. Wang, Y. et al. Gate-tunable negative longitudinal magnetoresistance in the predicted type-II Weyl semimetal WTe<sub>2</sub>. *Nat. Commun.* **7**, 13142 (2016).
54. Huang, X. et al. Observation of the Chiral-anomaly-induced negative magnetoresistance in 3D Weyl semimetal TaAs. *Phys. Rev. X* **5**, 031023 (2015).
55. Kim, H.-J. et al. Dirac versus Weyl fermions in topological insulators: Adler-Bell-Jackiw anomaly in transport phenomena. *Phys. Rev. Lett.* **111**, 246603 (2013).
56. Klotz, J. et al. Quantum oscillations and the Fermi surface topology of the Weyl semimetal NbP. *Phys. Rev. B* **93**, 121105 (2016).
57. Xiong, J. et al. Evidence for the chiral anomaly in the Dirac semimetal Na<sub>3</sub>Bi. *Science* **350**, 413–416 (2015).
58. Hosur, P. & Qi, X. Recent developments in transport phenomena in Weyl semimetals. *Comptes Rendus Phys.* **14**, 857–870 (2013).
59. Zhang, C. L. et al. Signatures of the Adler-Bell-Jackiw chiral anomaly in a Weyl fermion semimetal. *Nat. Commun.* **7**, 10735 (2016).
60. Hirschberger, M. et al. The chiral anomaly and thermopower of Weyl fermions in the half-Heusler GdPtBi. *Nat. Mater.* **15**, 1161–1165 (2016).
61. Brown, B. E. The crystal structures of WTe<sub>2</sub> and high-temperature MoTe<sub>2</sub>. *Acta Cryst.* **20**, 268–274 (1966).
62. Dawson, P. G. & Bullett, D. W. Electronic structure and crystallography of MoTe<sub>2</sub> and WTe<sub>2</sub>. *J. Phys. C: Solid State Phys.* **20**, 6159–6174 (1987).
63. Roushan, P. et al. Topological surface states protected from backscattering by chiral spin texture. *Nature* **460**, 1106–1109 (2009).
64. Fiete, G. A. & Heller, E. J. Theory of quantum corrals and quantum mirages. *Rev. Mod. Phys.* **75**, 933–948 (2003).
65. Wang, Q.-H. & Lee, D.-H. Quasiparticle scattering interference in high-temperature superconductors. *Phys. Rev. B* **67**, 020511 (2003).
66. Arguello, C. J. et al. Quasiparticle interference, quasiparticle interactions, and the origin of the charge density wave in 2H-NbSe<sub>2</sub>. *Phys. Rev. Lett.* **114**, 037001 (2015).
67. Kivelson, S. A. et al. How to detect fluctuating stripes in the high-temperature superconductors. *Rev. Mod. Phys.* **75**, 1201–1241 (2003).
68. Zhu, Z. H. et al. Rashba spin-splitting control at the surface of the topological insulator Bi<sub>2</sub>Se<sub>3</sub>. *Phys. Rev. Lett.* **107**, 186405 (2011).
69. Benia, H. M., Lin, C., Kern, K. & Ast, C. R. Reactive chemical doping of the Bi<sub>2</sub>Se<sub>3</sub> topological insulator. *Phys. Rev. Lett.* **107**, 177602 (2011).
70. Beidenkopf, H. et al. Spatial fluctuations of helical Dirac fermions on the surface of topological insulators. *Nat. Phys.* **7**, 939–943 (2011).
71. Baumberger, F. et al. Localization of surface states in disordered step lattices. *Phys. Rev. Lett.* **92**, 196805 (2004).
72. Kresse, G. & Furthmüller, J. Efficient iterative schemes for ab initio total-energy calculations using a plane-wave basis set. *Phys. Rev. B* **54**, 11169–11186 (1996).
73. Blöchl, P. E. Projector augmented-wave method. *Phys. Rev. B* **50**, 17953–17979 (1994).
74. Perdew, J. P., Burke, K. & Ernzerhof, M. Generalized gradient approximation made simple. *Phys. Rev. Lett.* **77**, 3865–3868 (1996).
75. Marzari, N. & Vanderbilt, D. Maximally localized generalized Wannier functions for composite energy bands. *Phys. Rev. B* **56**, 12847–12865 (1997).
76. Sancho, M. P. L., Sancho, J. M. L., Sancho, J. M. L. & Rubio, J. Highly convergent schemes for the calculation of bulk and surface Green functions. *J. Phys. F* **15**, 851–858 (1985).



**Open Access** This article is licensed under a Creative Commons Attribution 4.0 International License, which permits use, sharing, adaptation, distribution and reproduction in any medium or format, as long as you give appropriate credit to the original author(s) and the source, provide a link to the Creative Commons license, and indicate if changes were made. The images or other third party material in this article are included in the article's Creative Commons license, unless indicated otherwise in a credit line to the material. If material is not included in the article's Creative Commons license and your intended use is not permitted by statutory regulation or exceeds the permitted use, you will need to obtain permission directly from the copyright holder. To view a copy of this license, visit <http://creativecommons.org/licenses/by/4.0/>.

© The Author(s) 2018